nanomaterials

MDPI

Article

Large Scale Process for Low Crystalline MoO_3-Carbon Composite Microspheres Prepared by One-Step Spray Pyrolysis for Anodes in Lithium-Ion Batteries

Jung Sang Cho

Department of Engineering Chemistry, Chungbuk National University, Chungbuk 361-763, Korea; jscho@cbnu.ac.kr; Tel.: +82-43-261-2489; Fax: +82-43-262-2380

Received: 22 February 2019; Accepted: 27 March 2019; Published: 3 April 2019

Abstract: This paper introduces a large-scale and facile method for synthesizing low crystalline MoO_3/carbon composite microspheres, in which MoO_3 nanocrystals are distributed homogeneously in the amorphous carbon matrix, directly by a one-step spray pyrolysis. The MoO_3/carbon composite microspheres with mean diameters of 0.7 μm were directly formed from one droplet by a series of drying, decomposition, and crystalizing inside the hot-wall reactor within six seconds. The MoO_3/carbon composite microspheres had high specific discharge capacities of 811 mA h g^{-1} after 100 cycles, even at a high current density of 1.0 A g^{-1} when applied as anode materials for lithium-ion batteries. The MoO_3/carbon composite microspheres had final discharge capacities of 999, 875, 716, and 467 mA h g^{-1} at current densities of 0.5, 1.5, 3.0, and 5.0 A g^{-1}, respectively. MoO_3/carbon composite microspheres provide better Li-ion storage than do bare MoO_3 powders because of their high structural stability and electrical conductivity.

Keywords: molybdenum oxide; carbon composite; spray pyrolysis; anodes; lithium-ion batteries

1. Introduction

Lithium-ion batteries (LIBs) have been attractive as the most important type of power source for energy-storage system, electric vehicles, and other electronic devices because of their high specific capacities and energy densities [1–3]. Transition-metal oxides (TMOs) with high theoretical energy capacities have been widely applied as replacement anodes for the current graphite of LIBs [4–6]. However, the low intrinsic electric conductivity and the large volume expansion of TMOs during a charge/discharge cycle result in rapid capacity fading, which hinders the commercial application of TMOs for anodes in current LIBs [7,8]. To solve these problems, compositing TMOs with carbonaceous materials has been regarded as a possible solution. Carbon could effectively buffer the stress induced by the large volume change of TMOs during the fast charging–discharging process and improve the electrical conductivity of the anodes [9–11]. Additionally, a carbon matrix could prevent the aggregation of the active materials during repeated cycles by surrounding them, which increases the structural stability of anode materials [12,13]. Therefore, various synthesis strategies for TMOs/carbon composites have been introduced [14–18]. Cho et al. [14] prepared multiroom-structured metal–carbon hybrid microspheres containing empty voids of several tens of nanometers by liquid–liquid phase segregation because of the incongruent melting of the metal salt and dextrin during the spray pyrolysis. The discharge capacity of the multiroom-structured Co_3O_4–C hybrid microspheres for LIBs at a current density of 3 A g^{-1} for the 150th cycle was 1243 mA h g^{-1}. Zhang et al. [15] also prepared TiO_2–graphene composite nanofibers by a simple electrospinning process. The cell assembled with TiO_2–graphene composite nanofibers as an anode retained 84% of the reversible capacity after 300 cycles at a current density of 150 mA g^{-1}, which is 25% higher than bare TiO_2 nanofibers did under the same test

conditions. Bhaskar et al. [16] prepared MoO_2/multiwalled carbon nanotubes (MWCNTs) composed of spherical flowerlike nanostructures of MoO_2, interconnected by MWCNTs by a one-step hydrothermal route. The one-dimensional electron-transport pathways provided by MWCNTs, which are in direct contact with the MoO_2 nanostructures, imparted an improved reversible lithium storage capacity (1143 mA h g^{-1} at a current density of 100 mA g^{-1} after 200 cycles).

Molybdenum oxides are candidate anode materials for LIBs because MoO_3 exhibits good electrochemical properties, has a low cost, and is environmentally friendly [19–21]. Therefore, MoO_3 nanomaterials with diverse morphologies such as nanoparticles, hollow, nanobelts, naowiles, and porous structures have been prepared. Lee et al. [22] synthesized MoO_3 nanoparticles using hot filament chemical vapor deposition method (HFCVD) under an argon atmosphere. Zhao et al. [23] also synthesized MoO_3 hollow microspheres by a template-free solvothermal route and subsequent heat treatment in air. The MoO_3 hollow microspheres have a relatively high specific surface area. Chen et al. [24] prepared MoO_3 nanobelts by a hydrothermal method, in which the morphology of MoO_3 nanobelts was affected with the addition of PEG. MoO_{3-x} nanowires were prepared by Sunkara et al. [25] in a hot-filament chemical vapor deposition reactor. Ko et al. [26] prepared three-dimensional ordered macroporous structured MoO_3 by using a polystyrene bead template via ultrasonic spray pyrolysis.

In this study, low crystalline MoO_3/carbon composite microspheres, in which MoO_3 nanocrystals were distributed homogeneously in the amorphous C matrix, were directly prepared by one-step spray pyrolysis within several seconds. In here, MoO_3 was applied as the host material of carbon microspheres in this process because of its rich chemistry with multiple valence states, low electrical resistivity, high electrochemical activity toward lithium, and affordable cost. The resulting MoO_3/carbon composite microspheres worked better in terms of cycling and rate as anode materials for LIBs than did bare MoO_3 powders. The simple process introduced in this study is expected to be useful for the large-scale synthesis of TMOs/carbon composite microspheres as practical anode materials for LIBs. Furthermore, the synthesis strategy introduced is generally applied to synthesize various metal TMOs/carbon composites, including NiO, Co_3O_4, SnO_2, and Fe_2O_3, for a wide variety of applications including energy storage.

2. Materials and Methods

2.1. Sample Preparation

Low crystalline MoO_3/carbon composite microspheres, in which MoO_3 nanocrystals were distributed homogeneously in the amorphous C matrix, were directly prepared by a one-step spray pyrolysis. The spray pyrolysis system used in this study is shown in Figure S1. In brief, droplets were generated by a 1.7-MHz ultrasonic spray generator that consisted of six vibrators, and the droplets were carried to a quartz tube reactor (length = 1200 mm, diameter = 50 mm) by a flow of N_2 (flow rate = 5 L min^{-1}). The reactor temperature was fixed at 900 °C. The spray solution was prepared by dissolving 0.1 M of MoO_3 (98%, Sigma Aldrich, St. Louis, MO, USA), 12 g L^{-1} of polyvinylpyrrolidone (PVP, Mw 40,000, Daejung Chemicals and Metals, Siheung, Korea), and 0.02 M of sucrose in distilled water. Subsequently, an appropriate amount of hydrogen peroxide (30% H_2O_2, Sigma-Aldrich) was added to the above solution to obtain a clear spray solution. For the bare sample, MoO_3 powders without any carbon content were also prepared by spray pyrolysis. For this, the spray solution was prepared by dissolving 0.1 M of MoO_3 without a carbon precursor in H_2O_2 contained in distilled water. Subsequently, the spray pyrolysis was carried out with the prepared solution at a temperature of 900 °C by a flow of air (flow rate = 5 L min^{-1}).

2.2. Characterization Techniques

The microstructures of the resulting powders were observed by scanning electron microscopy (SEM; JEOL, JSM-6060, JEOL, Tokyo, Japan) and field-emission transmission electron microscopy

(FE-TEM; JEOL, JEM-2100F, JEOL, Tokyo, Japan). The crystal phases were evaluated by X-ray diffractometry (XRD; X'Pert PRO MPD, PANalytical, Almelo, The Netherlands) using Cu K_α radiation (λ = 1.5418 Å). X-ray photoelectron spectroscopy (XPS; K-Alpha, Thermo Fisher Scientific, Waltham, MA, USA) with a focused monochromatic Al K_α at 12 kV and 20 mA was used to analyze the composition of the samples. A structural characterization of carbon in the sample was performed by Raman spectra (Jobin Yvon LabRam HR800, Horiba Jobin Yvon, Paris, France, excited by a 632.8 nm He–Ne laser) at room temperature. The surface areas of the powders were measured by the Brunauer–Emmett–Teller (BET) method, using N_2 as the adsorbate gas. Thermogravimetric analyses (TGA) were performed using a Pyris 1 TGA (Perkin Elmer, Waltham, MA, USA) within a temperature range of 25–650 °C and at a heating rate of 10 °C min^{-1} under a static air atmosphere.

2.3. Electrochemical Measurements

The electrochemical properties of the samples were analyzed by constructing a 2032-type coin cell. The lithium cell assembly was made in an Ar-filled glove box at room temperature where water and the oxygen concentration was kept at less than 1 ppm. The anode slurry was prepared by mixing the active material, carbon black, and sodium carboxymethyl cellulose (CMC) in a weight ratio of 7:2:1. The working electrodes were formed by coating the slurry onto copper foils and subsequently dried at 70 °C for 3 h. Li metal and a microporous polypropylene film were used as the counter electrode and the separator, respectively. The electrolyte was composed of 1 M $LiPF_6$ dissolved in a mixture of fluoroethylene carbonate/dimethyl carbonate (FEC/DMC; 1:1 v/v). The discharge/charge characteristics of the samples were investigated by cycling over a potential range of 0.001–3.0 V under CC (constant-current) conditions. Cyclic voltammograms were measured at a scan rate of 0.1 mV s^{-1}. The negative electrode measured 1.5 cm × 1.5 cm, and the mass loading of the active materials was kept at approximately 1.5 mg cm^{-2} in every electrochemical test. The electrochemical impedance spectra were obtained by performing alternating current electrochemical impedance spectroscopy (EIS; ZIVE SP1) over a frequency range of 0.01 Hz to 100 kHz.

3. Results and Discussion

Low crystalline MoO_3/C composite microspheres, in which MoO_3 nanocrystals were distributed homogeneously in the amorphous C matrix, were directly prepared by a one-step spray pyrolysis without any further treatment. Figure 1 shows the morphologies of the MoO_3/C composite microspheres obtained after the one-step spray pyrolysis. The powders were spherical and had diameters on the order of microns because they were formed from one droplet with several tens of micrometers by drying, decomposition, and crystallization inside the hot-wall reactor, as shown in Scheme 1. Additionally, there was no aggregation between the powders because the spray pyrolysis was carried out within a very short residence time of 6 s in a hot-wall reactor maintained at 900 °C under a N_2 atmosphere in Figure 1a,b. From a high-resolution TEM image in Figure 1c, it was hard to confirm the nanocrystal MoO_3 grains formed during spray pyrolysis in a microsphere structure because the amorphous-like, very small MoO_3 nanocrystals were formed during the spray pyrolysis at 900 °C within a short residence time of 6 s. The XRD result also showed the broad peak intensities of the β-MoO_3 phase in Figure 1d. The mean crystallite size of the MoO_3 powders, which was calculated from the width of the (011) peak using Scherrer's equation, was 4 nm. Grain growth of the MoO_3 nanocrystals was effectively prohibited both by the short residence time of the droplet in the reactor and by being surrounded by the carbon formed by the decomposition of PVP and sucrose during the process. The elemental mapping images shown in Figure 1e exhibited a homogeneous distribution of Mo, O, and C, which implies that the ultrafine MoO_3 nanocrystals were homogeneously composited with C in the microsphere structure.

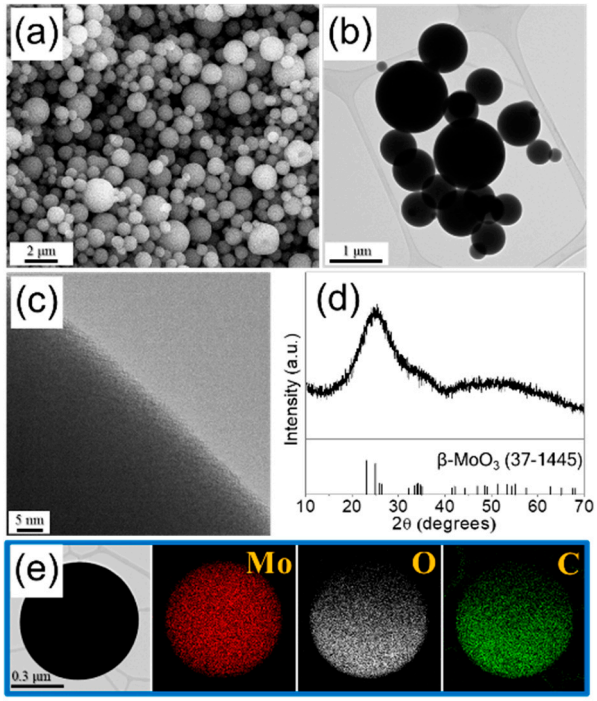

Figure 1. The (**a**) SEM, (**b**) TEM, (**c**) high-resolution TEM images, (**d**) XRD pattern, and (**e**) elemental mapping images of MoO_3/C composite microspheres.

Scheme 1. The formation mechanism of the low crystalline MoO_3/C composite microspheres by the one-step spray pyrolysis process.

To identify the chemical composition of the MoO_3/C composite microspheres, XPS analysis was carried out, as shown in Figure 2. The XPS survey spectrum of the composite microspheres confirmed the presence of Mo, O, and C, as shown in Figure 2a. In the Mo 3d spectrum of the microspheres (Figure 2b), the main peaks occurred at binding energies of 231.7/232.7 eV for Mo 3d5/2 and 234.7/235.7 eV for Mo 3d3/2; the peaks located at 232.7 and 235.7 eV are characteristic of typical values of the 3d orbital doublet Mo^{6+}, and the minor ones centered on 231.7 and 234.7 eV corresponded to the 3d orbital doublet Mo^{5+}, which indicated that dangling bond sites where charges could be trapped existed in MoO_3 [27,28]. The C 1s XPS peak observed at 284.6 eV in Figure 2d corresponds to the binding energy of the sp^2 C–C bond of the carbon matrix [29–31].

The carbon matrix of the MoO_3/C composite microspheres was characterized by means of Raman spectroscopy. The degree of graphitization of the carbon material can typically be evaluated according to the intensity ratio of the D and G bands of carbon at approximately 1350 and 1590 cm^{-1}, respectively [32,33]. The peak intensity ratio between the D and G bands (I_D/I_G) for the MoO_3/C composite microspheres was approximately 3.2, and the absence of the 2D band at approx. 2685 cm^{-1} demonstrated that the carbon formed in the composite was fairly disordered. Thus, a large amount

of the amorphous carbon was formed by the decomposition of both PVP and sucrose during the spray pyrolysis. In general, amorphous carbon has more capacity as an anode for LIBs than graphitic carbon, which is mainly contributed by pores and voids in the microcavities of the structure. The Thermogravimetric (TG) curve of the MoO_3/C composite microspheres in Figure 3b revealed a weight loss between 380 and 460 °C because of the degradation of amorphous carbon. Therefore, the content of amorphous carbon of the MoO_3/C composite microspheres estimated from the TG analysis was 26 wt %.

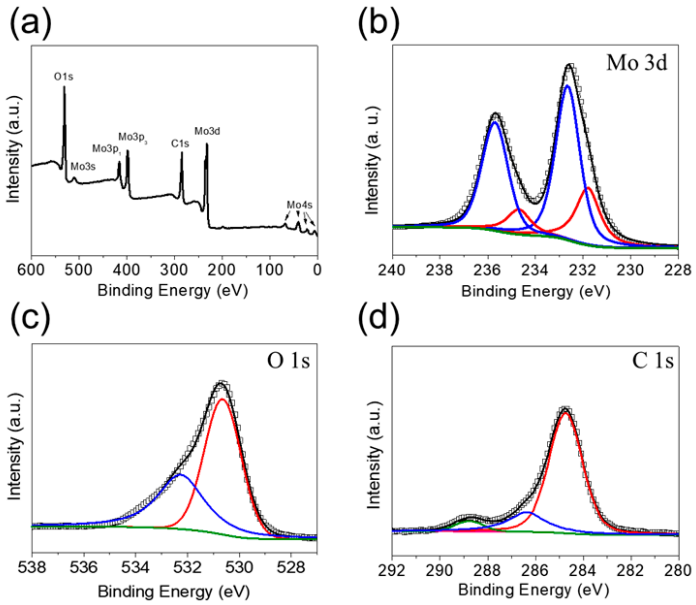

Figure 2. The XPS spectra of the MoO_3/C composite microspheres: (**a**) the survey XPS spectrum and high-resolution XPS spectra of (**b**) Mo 3d, (**c**) O 1S, and (**d**) C 1s.

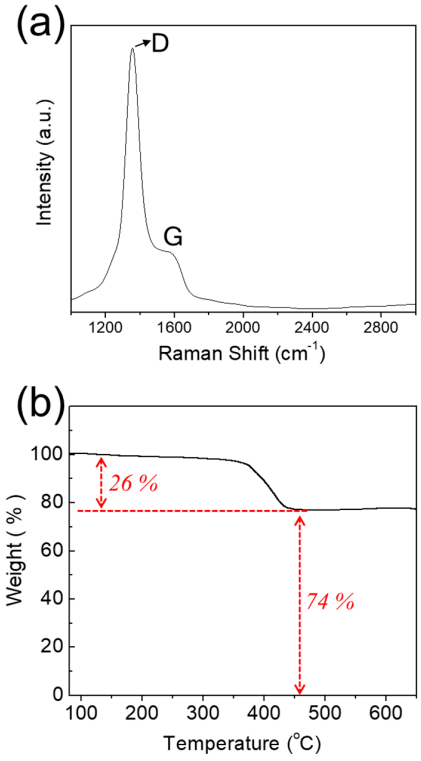

Figure 3. (**a**) The Raman spectrum and (**b**) thermogravimetric analysis (TGA) curve of the MoO_3/C composite microspheres.

In order to clearly prove the structural merits of MoO_3/C composite microspheres as anodes for Li^+ ion storage properties, bare MoO_3 powders without C were also prepared from the spray solution without either PVP and sucrose by spray pyrolysis, as shown in Figure 4. The mean particle size of the resulting bare MoO_3 powders, as measured from the SEM and TEM images in Figure 4a,b, was 420 nm and had no aggregation between the powders. Additionally, the resulting powders were angular, which is attributed to the crystal growth of MoO_3 particles because there was no carbon surrounding the particles during spray pyrolysis to prevent the growth of MoO_3 crystals during the short residence reaction time of the droplets. The high-resolution TEM image in Figure 4c shows clear lattice fringes separated by 0.23 nm, which corresponds to the (011) crystal plane of β-MoO_3 (JCPDS card No. 37–1445) [34]. The XRD pattern of the bare MoO_3 powders (Figure 4d) shows that they have different allotropes of MoO_3 structures, with no impurities. The thermodynamically favored α-MoO_3 phase was newly formed along with β-MoO_3 in the bare MoO_3 powders during spray pyrolysis. Bare MoO_3 powders without C were further confirmed by the elemental mapping images in Figure 4e. The BET surface areas of the MoO_3/C composite microspheres and of the bare MoO_3 powders were 4.3 and 0.6 $m^2\ g^{-1}$, respectively, in Figure S2.

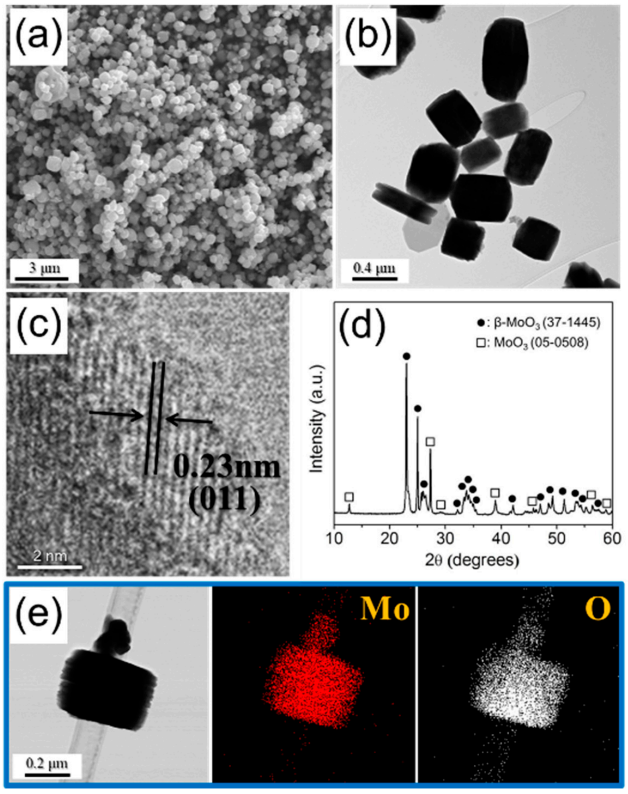

Figure 4. The (**a**) SEM, (**b**) TEM, (**c**) high-resolution TEM images, (**d**) XRD pattern, and (**e**) elemental-mapping images of the bare MoO_3 powders.

The electrochemical properties of the MoO_3/C composite microspheres are compared with those of the bare MoO_3 powders in Figure 5. The cyclic voltammogram (CV) curves of the MoO_3/C composite microspheres and bare MoO_3 powders performed in the 0.01–3.0 V range at a scanning rate of 0.01 mV s^{-1} for the first four cycles are shown in Figure 5a. In the first cathodic scan of the MoO_3/C composite microspheres, the broad peaks located at 1.16 V and 0.21 V are assigned to the interaction of Li^+ ions with the amorphous carbon matrix of the MoO_3/C composite and conversion reaction of Li_xMoO_3 to Mo_0 and Li_2O [35–37]. The peak at 0.05 V is also observed, caused by the Li^+ ion's intercalation into the C matrix [38,39]. In the anodic scans of the MoO_3/C composite microspheres, reversible peaks at 1.42 and 1.77 V are attributed to the monoclinic-orthorhombic-monoclinic phase

transitions in the partially lithiated Li_xMoO_2 [35–37]. In the subsequent cycles, two redox peak pairs appeared at 0.21/1.3 and 1.42/1.77 V, which corresponded to the redox reaction of MoO_3 [35,40,41]. The bare MoO_3 powders showed peaks at 2.03 and 1.8 V in the first cathodic scan, which correspond to the generation of Li_xMoO_3, causing an irreversible structural change from the α-MoO_3 additionally formed in the bare MoO_3 powders to an amorphous phase [40–42]. The subsequent peak at 0.17 V results from the conversion reaction of Li_xMoO_3 to Mo_0 and Li_2O [35–37,41].

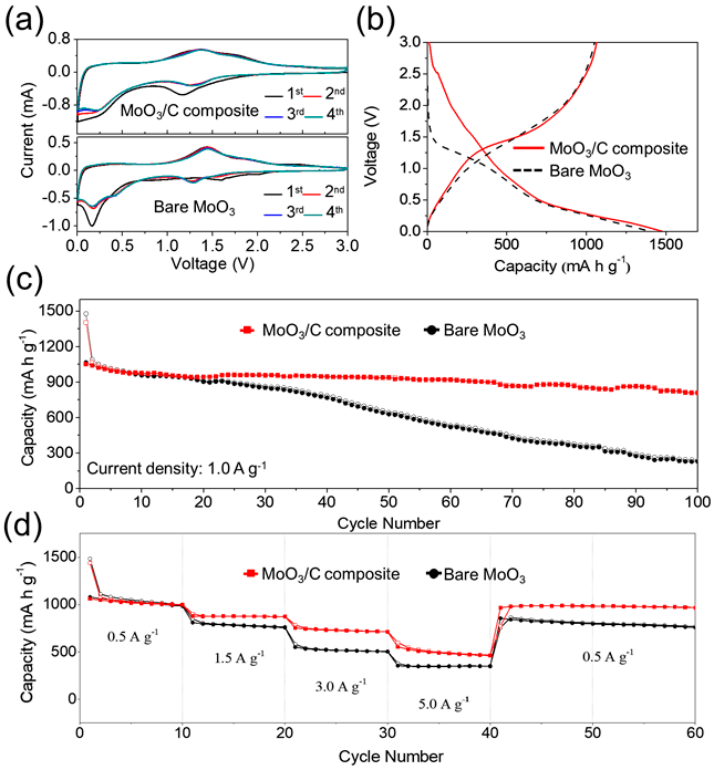

Figure 5. The electrochemical properties of the MoO_3/C composite microspheres and the bare MoO_3 powders: (**a**) CV curves, (**b**) charge-discharge curves, (**c**) cycling performances, and (**d**) rate performances.

The initial discharge-charge curves of the two samples at a current density of 1.0 A g^{-1} are shown in Figure 5b. The initial discharge capacities of the MoO_3/C composite microspheres and the bare MoO_3 powders were 1403 mA h g^{-1} and 1478 mA h g^{-1}, respectively, and their initial Coulombic efficiencies were 75% and 72%, respectively. Although the MoO_3/C composite microspheres contained C with a high irreversible capacity loss, the initial Coulombic efficiency of the MoO_3/C composite microspheres was relatively higher than that of the bare MoO_3 powders. The high structural damage to the bare MoO_3 powders in the first discharge and charge processes resulted in a low initial Coulombic efficiency. The discharge capacity and cycling properties of the MoO_3/C composite microspheres and bare MoO_3 powders at a current density of 1.0 A g^{-1} are shown in Figure 5c. Compared with bare MoO_3 powders, the MoO_3/C composite microspheres exhibited a satisfactorily stable cycling performance. The discharge capacity of the MoO_3/C composite microspheres decreased slightly from 1066 mA h g^{-1} (533 mA h cc^{-1}) to 808 mA h g^{-1} (404 mA h cc^{-1}) from the 2nd cycle to the 100th cycle, whereas that of the bare MoO_3 powders decreased rapidly from 1090 mA h g^{-1} (621 mA h cc^{-1}) to 239 mA h g^{-1} (136 mA h cc^{-1}) in the same cycle range. Additionally, the Coulombic efficiency of the MoO_3/C composite microspheres increased quickly to above 99% after the second cycle. The amorphous C matrix of MoO_3/C composite microspheres more effectively buffered the large volume change of the MoO_3 active material during the fast charging–discharging process. On the other hand, the structural destruction of the bare MoO_3 powders during repeated Li^+-ion insertion and

desertion processes resulted in capacity fading continuously. Therefore, better cycling of the MoO_3/C composite microspheres could be achieved because of the improved structural stability of the MoO_3.

In order to evaluate the rate performances of both samples, electrochemical tests were performed at various current densities, as shown in Figure 5d. As the current densities increased from 0.5 to 1.5, 3.0, and 5.0 A g^{-1}, the MoO_3/C composite microspheres exhibited reversible discharge capacities of 999, 875, 716, and 467 mA h g^{-1}, respectively. However, the bare MoO_3 powders delivered a low reversible discharge capacity of 352 mA h g^{-1} at 5.0 A g^{-1} as shown in Figure 5d. The C matrix of the MoO_3/C composite microspheres improved the electrical conductivity of the sample. Additionally, the small, amorphous MoO_3 nanograins imbedded within the C matrix decreased the diffusion distance and increased the diffusion rate of the Li^+ ions, thus synergistically speeding up the rate of the MoO_3/C composite microspheres more than that of the bare MoO_3 powders.

The superior Li^+-ion storage properties of the MoO_3/C composite microspheres were supported by EIS analysis, as shown in Figure 6 [43–45]. Nyquist plots of the samples before and after cycles were obtained by deconvolution with a Randle-type equivalent-circuit model (Figure 6d). The MoO_3/C composite microspheres and bare MoO_3 powders had similar charge-transfer resistance (Rct) values before cycling, as shown in Figure 6a. However, the cell with the MoO_3/C composite microspheres obtained after 100 cycles showed a lower Rct value of 42 Ω compared to that of 134 Ω for the bare MoO_3 powders, as shown in Figure 6b,c. The structural destruction of the bare MoO_3 powders during the repeated Li^+-ion insertion and desertion processes increased the Rct values significantly. On the other hand, the MoO_3 nanograins embedded within the amorphous C were not pulverized during the repeated cycles. Moreover, the C matrix served as fast and continuous transport pathways for electrons upon cycling because of its high electrical conductivity. The high structural stabilities of the MoO_3/C composite microspheres with high lithium-ion storage capacities resulted in low Rct values during cycling. The MoO_3/C composite microspheres with a high structural stability during repeated lithium insertion and desertion reactions showed excellent cycling and rate performance, as shown in Figure 5.

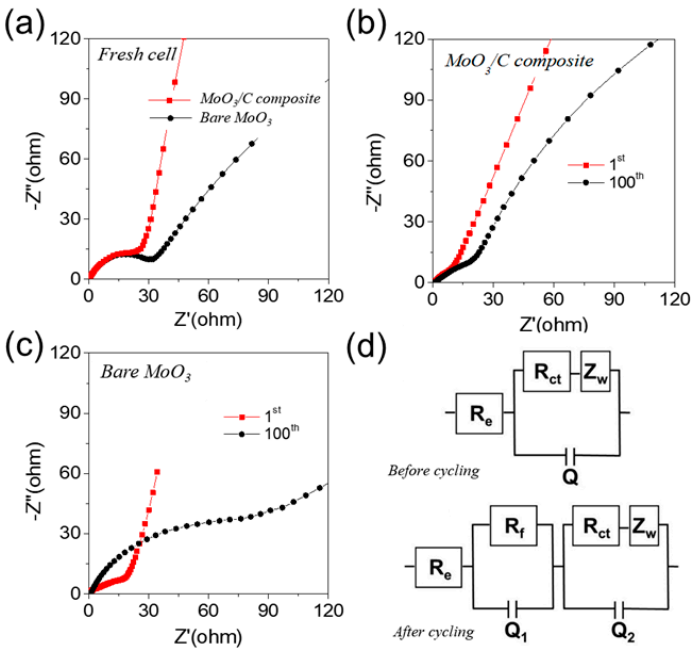

Figure 6. The impedance analysis of the MoO_3/C composite microspheres and the bare MoO_3 powders: (**a**) before cycling, (**b**) bare MoO_3 powders, (**c**) MoO_3/C composite microspheres, and (**d**) the tquivalent circuit model used for AC impedance fitting: R_{ct} = charge-transfer resistance, R_e = electrolyte resistance, R_f = SEI layer resistance, Q_1 = dielectric relaxation capacitance, and Q_2 = associated double layer capacitance.

The morphologies of the MoO_3/C composite microspheres and bare MoO_3 powders obtained after 100 cycles are shown in Figure 7. The bare MoO_3 powders were broken into several pieces after the cycles, as shown by the TEM image in Figure 7a. In contrast, the MoO_3/C composite microspheres maintained their morphologies quite well even after the repeated Li^+ insertion and desertion processes in Figure 7b,c. The excellent Li^+-ion storage properties of the MoO_3/C composite microspheres are, therefore, attributed to the improvement of the structural stability and electrical conductivity by the carbon composite.

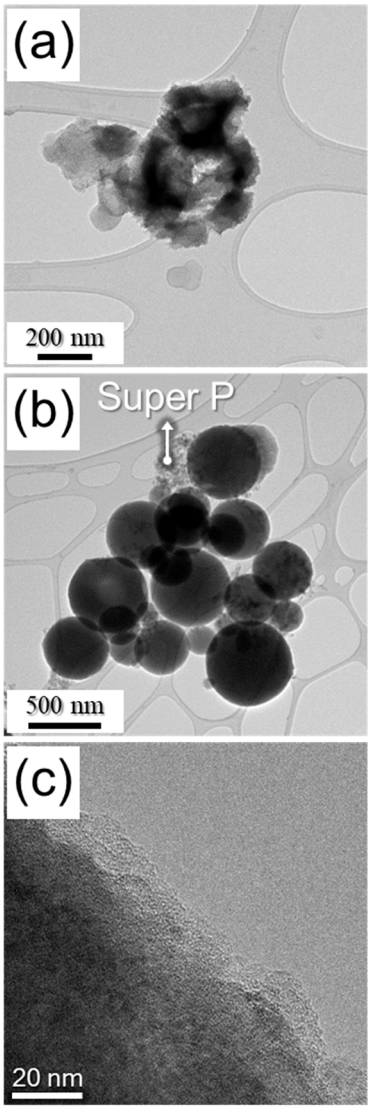

Figure 7. The morphologies of (**a**) bare MoO_3 powders and (**b**,**c**) MoO_3/C composite microspheres obtained after 100 cycles at a constant current density of 1.0 A g^{-1}.

4. Conclusions

In this study, low crystalline MoO_3/carbon composite microspheres in which MoO_3 nanocrystals were distributed homogeneously in the amorphous C matrix, were directly prepared by a one-step spray pyrolysis within several seconds. The MoO_3/carbon composite was spherical, with diameters on the order of microns, because they were formed from one droplet with several tens of micrometers by a series of drying, decomposition, and crystallization processes inside the hot-wall reactor during spray pyrolysis. The amorphous C matrix of the MoO_3/C composite microspheres effectively buffered the large volume change of the MoO_3 active material during the fast charging–discharging process.

Therefore, a better cycling of the MoO_3/C composite microspheres could be achieved because of the improved structural stability of the MoO_3. Additionally, the small MoO_3 nanograins imbedded within the C matrix decreased the diffusion distance and increased the diffusion rate of Li^+ ions, thus accelerating the rate of the MoO_3/C composite microspheres. The superior Li^+-ion storage properties of the MoO_3/C composite microspheres compared to those of the bare MoO_3 were supported by an EIS analysis and by observing the morphologies of the samples obtained after 100 cycles. The simple process introduced in this study is expected to be useful for the large-scale synthesis of TMOs/carbon composite microspheres for a wide variety of applications including energy storage.

Supplementary Materials: The following are available online at http://www.mdpi.com/2079-4991/9/4/539/s1, Figure S1: Schematic diagram of spray pyrolysis system applied in the preparation of MoO_3/C composite microspheres, Figure S2: N_2 adsorption-desorption isotherms measured at 77 K for the MoO_3/C composite microspheres and bare MoO_3 powders, Figure S3: Cycle properties of the MoO_3/C composite microspheres and the bare MoO_3 powders, Figure S4: TGA curve of the bare MoO_3 powders, Table S1: Fitted data obtained from the equivalent circuit for Nyquist plots.

Funding: This work was supported by the National Research Foundation of Korea (NRF) grant funded by the Korea government (MSIP) (NRF-2018R1A4A1024691, NRF-2017M1A2A2087577, and NRF-2018R1D1A3B07042514).

Conflicts of Interest: The authors declare no conflict of interest.

References

1. Chen, X.; Wang, Z.; Zhang, R.; Xu, L.; Sun, D. A novel polyoxometalate-based hybrid containing a 2D $[CoMo_8O_{26}]_\infty$ structure as the anode for lithium-ion batteries. *Chem. Commun.* **2017**, *53*, 10560–10563. [CrossRef]
2. Lin, H.B.; Rong, H.B.; Huang, W.Z.; Liao, Y.H.; Xing, L.D.; Xu, M.Q.; Li, X.P.; Li, W.S. Triple-shelled Mn_2O_3 hollow nanocubes: Force-induced synthesis and excellent performance as the anode in lithium-ion batteries. *J. Mater. Chem. A* **2014**, *2*, 14189–14194. [CrossRef]
3. Zhu, Z.; Wang, S.; Du, J.; Jin, Q.; Zhang, T.; Cheng, F.; Chen, J. Ultrasmall Sn nanoparticles embedded in nitrogen-doped porous carbon as high-performance anode for lithium-ion batteries. *Nano Lett.* **2013**, *14*, 153–157. [CrossRef]
4. Bai, Z.; Zhang, Y.; Zhang, Y.; Guo, C.; Tang, B.; Sun, D. MOFs-derived porous Mn_2O_3 as high-performance anode material for Li-ion battery. *J. Mater. Chem. A* **2015**, *3*, 5266–5269. [CrossRef]
5. Cui, L.; Shen, J.; Cheng, F.; Tao, Z.; Chen, J. SnO_2 nanoparticles@ polypyrrole nanowires composite as anode materials for rechargeable lithium-ion batteries. *J. Power Sources* **2011**, *196*, 2195–2201. [CrossRef]
6. Zhong, X.; Huan, H.; Liu, X.; Yu, Y. Facile synthesis of porous germanium-iron bimetal oxide nanowires as anode materials for lithium-ion batteries. *Nano Res.* **2018**, *11*, 3702–3709. [CrossRef]
7. Jin, L.; Qiu, Y.; Deng, H.; Li, W.; Li, H.; Yang, S. Hollow $CuFe_2O_4$ spheres encapsulated in carbon shells as an anode material for rechargeable lithium-ion batteries. *Electrochim. Acta* **2011**, *56*, 9127–9132. [CrossRef]
8. Wang, Y.; Xu, J.; Wu, H.; Xu, M.; Peng, Z.; Zheng, G. Hierarchical SnO_2–Fe_2O_3 heterostructures as lithium-ion battery anodes. *J. Mater. Chem.* **2012**, *22*, 21923–21927. [CrossRef]
9. Han, F.; Li, D.; Li, W.-C.; Lei, C.; Sun, Q.; Lu, A.-H. Nanoengineered polypyrrole-coated Fe_2O_3@C multifunctional composites with an improved cycle stability as lithium-ion anodes. *Adv. Funct. Mater.* **2013**, *23*, 1692–1700. [CrossRef]
10. Huang, X.H.; Tu, J.P.; Zhang, C.Q.; Chen, X.T.; Yuan, Y.F.; Wu, H.M. Spherical NiO-C composite for anode material of lithium ion batteries. *Electrochim. Acta* **2007**, *52*, 4177–4181. [CrossRef]
11. Jo, M.S.; Ghosh, S.; Jeong, S.M.; Kang, Y.C.; Cho, J.S. Coral-like yolk–shell-structured nickel oxide/carbon composite microspheres for high-performance Li-ion storage anodes. *Nano-Micro Lett.* **2019**, *11*, 3. [CrossRef]
12. Li, L.; Li, Z.; Fu, W.; Li, F.; Wang, J.; Wang, W. α-Fe_2O_3@C nanorings as anode materials for high performance lithium ion batteries. *J. Alloy. Compd.* **2015**, *647*, 105–109. [CrossRef]
13. Park, G.D.; Kim, J.H.; Park, S.-K.; Kang, Y.C. $MoSe_2$ embedded CNT-reduced graphene oxide composite microsphere with superior sodium ion storage and electrocatalytic hydrogen evolution performances. *ACS Appl. Mater. Interfaces* **2017**, *9*, 10673–10683. [CrossRef]

14. Cho, J.S.; Won, J.M.; Lee, J.-K.; Kang, Y.C. Design and synthesis of multiroom-structured metal compounds–carbon hybrid microspheres as anode materials for rechargeable batteries. *Nano Energy* **2016**, *26*, 466–478. [CrossRef]
15. Zhang, X.; Suresh Kumar, P.; Aravindan, V.; Liu, H.H.; Sundaramurthy, J.; Mhaisalkar, S.G.; Duong, H.M.; Ramakrishna, S.; Madhavi, S. Electrospun TiO_2–graphene composite nanofibers as a highly durable insertion anode for lithium ion batteries. *J. Phys. Chem. C* **2012**, *116*, 14780–14788. [CrossRef]
16. Bhaskar, A.; Deepa, M.; Narasinga Rao, T. MoO_2/multiwalled carbon nanotubes (MWCNT) hybrid for use as a Li-ion battery anode. *ACS Appl. Mater. Interfaces* **2013**, *5*, 2555–2566. [CrossRef] [PubMed]
17. Cho, J.S.; Hong, Y.J.; Kang, Y.C. Design and synthesis of bubble-nanorod-structured Fe_2O_3–carbon nanofibers as advanced anode material for Li-ion batteries. *ACS Nano* **2015**, *9*, 4026–4035. [CrossRef]
18. Park, S.-K.; Park, G.D.; Kang, Y.C. Three-dimensional porous microspheres comprising hollow Fe_2O_3 nanorods/CNT building blocks with superior electrochemical performance for lithium ion batteries. *Nanoscale* **2018**, *10*, 11150–11157. [CrossRef]
19. Whittingham, M.S. The role of ternary phased in cathode reactions. *Electrochem. Soc.* **1976**, *123*, 315–320. [CrossRef]
20. Choi, S.H.; Kang, Y.C. Crumpled graphene–molybdenum oxide composite powders: Preparation and application in lithium-ion batteries. *ChemSusChem* **2014**, *7*, 523–528. [CrossRef]
21. Xue, X.Y.; Chen, Z.H.; Xing, L.L.; Yuan, S.; Chen, Y.J. SnO2/a-MoO3 core-shell nanobelts and their extraordinarily high reversible capacity as lithium-ion battery anodes. *Chem. Commun.* **2011**, *47*, 5205–5207. [CrossRef] [PubMed]
22. Lee, S.H.; Kim, Y.H.; Deshpande, R.; Parilla, P.A.; Whitney, E.; Gillaspie, D.T.; Kim, M.J.; Mahan, A.H.; Zhang, S.B.; Dillon, A.C. Reversible lithium-ion insertion in molybdenum oxide nanoparticles. *Adv. Mater.* **2008**, *20*, 3627–3632. [CrossRef]
23. Zhao, X.; Cao, M.; Hu, C. Thermal oxidation synthesis hollow MoO3 microspheres and their applications in lithium storage and gas-sensing. *Mater. Res. Bull.* **2013**, *48*, 2289–2295. [CrossRef]
24. Mohan, V.M.; Bin, H.; Chen, W. Enhancement of electrochemical properties of MoO3 nanobelts electrode using PEG as surfactant for lithium battery. *J. Solid State Electrochem.* **2010**, *14*, 1769–1775. [CrossRef]
25. Meduri, P.; Clark, E.; Kim, J.H.; Dayalan, E.; Sumanasekera, G.U.; Sunkara, M.K. MoO3–x nanowire arrays as stable and high-capacity anodes for lithium ion batteries. *Nano Lett.* **2012**, *12*, 1784–1788. [CrossRef] [PubMed]
26. Ko, Y.N.; Park, S.B.; Jung, K.Y.; Kang, Y.C. One-pot facile synthesis of ant-cave- structured metal oxide-carbon microballs by continuous process for use as anode materials in Li-ion batteries. *Nano Lett.* **2013**, *13*, 5462–5466. [CrossRef]
27. Xie, F.; Choy, W.C.H.; Wang, C.; Li, X.; Zhang, S.; Hou, J. Low-temperature solution-processed hydrogen molybdenum and vanadium bronzes for an efficient hole-transport layer in organic electronics. *Adv. Mater.* **2013**, *25*, 2051–2055. [CrossRef]
28. Zhu, Y.; Yuan, Z.; Cui, W.; Wu, Z.; Sun, Q.; Wang, S.; Kang, Z.; Sun, B. A cost-effective commercial soluble oxide cluster for highly efficient and stable organic solar cells. *J. Mater. Chem. A* **2014**, *2*, 1436–1442. [CrossRef]
29. Kim, J.H.; Oh, Y.J.; Kang, Y.C. Design and synthesis of macroporous ($Mn_{1/3}Co_{2/3}$)O-carbon nanotubes composite microspheres as efficient catalysts for rechargeable Li-O_2 batteries. *Carbon* **2018**, *128*, 125–133. [CrossRef]
30. Park, G.D.; Lee, J.-K.; Kang, Y.C. Three-dimensional macroporous CNTs microspheres highly loaded with $NiCo_2O_4$ hollow nanospheres showing excellent lithium-ion storage performances. *Carbon* **2018**, *128*, 191–200. [CrossRef]
31. Liu, S.-Y.; Xie, J.; Pan, Q.; Wu, C.-Y.; Cao, G.-S.; Zhu, T.-J.; Zhao, X.-B. Graphene anchored with nanocrystal Fe_2O_3 with improved electrochemical Li-storage properties. *Int. J. Electrochem. Sci.* **2012**, *7*, 354–362.
32. Cho, J.S.; Lee, S.Y.; Kang, Y.C. First introduction of $NiSe_2$ to anode material for sodium-ion batteries: A hybrid of graphene-wrapped $NiSe_2$/C porous nanofiber. *Sci. Rep.* **2016**, *6*, 23338. [CrossRef] [PubMed]
33. Bhattacharya, K.; Gogoi, B.; Buragohain, A.K.; Deb, P. Fe_2O_3/C nanocomposites having distinctive antioxidant activity and hemolysis prevention efficiency. *Mater. Sci. Eng. C* **2014**, *42*, 595–600. [CrossRef]
34. Shakir, I.; Shahid, M.; Kang, D.J. MoO_3 and $Cu_{0.33}MoO_3$ nanorods for unprecedented UV/visible light photocatalysis. *Chem. Commun.* **2010**, *46*, 4324–4326. [CrossRef] [PubMed]

35. Sen, U.K.; Mitra, S. Synthesis of molybdenum oxides and their electrochemical properties against Li. *Energy Procedia* **2014**, *54*, 740–747. [CrossRef]
36. Yu, Z.; Jiang, H.; Gu, D.; Li, J.; Wang, L.; Shen, L. A new way to prepare MoO_3/C as anode of lithium ion battery for enhancing the electrochemical performance at room temperature. *J. Electrochem. Sci. Technol.* **2016**, *7*, 170–178. [CrossRef]
37. Zhou, J.; Lin, N.; Wang, L.; Zhang, K.; Zhu, Y.; Qian, Y. Synthesis of hexagonal MoO_3 nanorods and a study of their electrochemical performance as anode materials for lithium-ion batteries. *J. Mater. Chem. A* **2015**, *3*, 7463–7468. [CrossRef]
38. Ji, L.; Lin, Z.; Guo, B.; Medford, A.J.; Zhang, X. Assembly of carbon–SnO_2 core–sheath composite nanofibers for superior lithium storage. *Chem.-Eur. J.* **2010**, *16*, 11543–11548. [CrossRef]
39. Oh, S.H.; Kim, J.K.; Kang, Y.C.; Cho, J.S. Three-dimensionally ordered mesoporous multicomponent (Ni, Mo) metal oxide/N-doped carbon composite with superior Li-ion storage performance. *Nanoscale* **2018**, *10*, 18734–18741. [CrossRef] [PubMed]
40. Wu, D.; Shen, R.; Yang, R.; Ji, W.; Jiang, M.; Ding, W.; Peng, L. Mixed molybdenum oxides with superior performances as an advanced anode material for lithium-ion batteries. *Sci. Rep.* **2017**, *7*, 44697. [CrossRef] [PubMed]
41. Zhao, G.; Zhang, N.; Sun, K. Electrochemical preparation of porous MoO_3 film with a high rate performance as anode for lithium ion batteries. *J. Mater. Chem. A* **2013**, *1*, 221–224. [CrossRef]
42. Xia, Q.; Zhao, H.; Du, Z.; Zeng, Z.; Gao, C.; Zhang, Z.; Du, X.; Kulka, A.; Świerczek, K. Facile synthesis of MoO_3/carbon nanobelts as high-performance anode material for lithium ion batteries. *Electrochim. Acta* **2015**, *180*, 947–956. [CrossRef]
43. Lee, J.H.; Oh, S.H.; Jeong, S.Y.; Kang, Y.C.; Cho, J.S. Rattle-type porous Sn/C composite fibers with uniformly distributed nanovoids containing metallic Sn nanoparticles for high-performance anode materials in lithium-ion batteries. *Nanoscale* **2018**, *10*, 21483–21491. [CrossRef] [PubMed]
44. Ma, X.-H.; Feng, X.-Y.; Song, C.; Zou, B.-K.; Ding, C.-X.; Yu, Y.; Chen, C.-H. Facile synthesis of flower-like and yarn-like α-Fe_2O_3 spherical clusters as anode materials for lithium-ion batteries. *Electrochim. Acta* **2013**, *93*, 131–136. [CrossRef]
45. Wang, Y.; Xu, M.; Peng, Z.; Zheng, G. Direct growth of mesoporous Sn-doped TiO_2 thin films on conducting substrates for lithium-ion battery anodes. *J. Mater. Chem. A* **2013**, *1*, 13222–13226. [CrossRef]

© 2019 by the author. Licensee MDPI, Basel, Switzerland. This article is an open access article distributed under the terms and conditions of the Creative Commons Attribution (CC BY) license (http://creativecommons.org/licenses/by/4.0/).